26. Gao, R. S. *et al.* Evidence that nitric acid increases relative humidity in low-temperature cirrus clouds. *Science* **303,** 516–520 (2004).
27. Chang, H. Y. A., Koop, T., Molina, L. T. & Molina, M. J. Phase transitions in emulsified HNO_3/H_2O and $HNO_3/H_2SO_4/H_2O$ solutions. *J. Phys. Chem. A* **103,** 2673–2679 (1999).
28. Koop, T., Kapilashrami, A., Molina, L. T. & Molina, M. J. Phase transitions of sea-salt/water mixtures at low temperatures: Implications for ozone chemistry in the polar marine boundary layer. *J. Geophys. Res.* **105,** 26393–26402 (2000).
29. Bertram, A. K., Koop, T., Molina, L. T. & Molina, M. J. Ice formation in $(NH_4)_2SO_4$-H_2O particles. *J. Phys. Chem. A* **104,** 584–588 (2000).
30. Koop, T., Luo, B. P., Tsias, A. & Peter, T. Water activity as the determinant for homogeneous ice nucleation in aqueous solutions. *Nature* **406,** 611–614 (2000).

Acknowledgements We thank D. M. Murphy for several helpful discussions on cubic ice, G. N. Patey for discussions on theoretical calculations, and A. Lam and B. Patrick for their assistance with X-ray diffraction measurements and interpretation. We are also grateful to M. Raudsepp for discussions on crystallography. This research was supported by the Canadian Foundation for Climate and Atmospheric Sciences, the Natural Sciences and Engineering Research Council of Canada, and the Canadian Foundation for Innovation.

Competing interests statement The authors declare that they have no competing financial interests.

Correspondence and requests for materials should be addressed to A.K.B (bertram@chem.ubc.ca).

Measuring the onset of locking in the Peru–Chile trench with GPS and acoustic measurements

Katie Gagnon[1], C. David Chadwell[1] & Edmundo Norabuena[2]

[1]*Scripps Institution of Oceanography, Marine Physical Lab, San Diego, California 92093-0205, USA*
[2]*Geodesy Department, University of Miami, Miami, Florida 33149, USA*

The subduction zone off the west coast of South America marks the convergence of the oceanic Nazca plate and the continental South America plate. Nazca–South America convergence over the past 23 million years has created the 6-km-deep Peru–Chile trench, 150 km offshore. High pressure between the plates creates a locked zone, leading to deformation of the overriding plate. The surface area of this locked zone is thought to control the magnitude of co-seismic release and is limited by pressure, temperature, sediment type and fluid content[1]. Here we present seafloor deformation data from the submerged South America plate obtained from a combination of Global Positioning System (GPS) receivers and acoustic transponders. We estimate that the measured horizontal surface motion perpendicular to the trench is consistent with a model having no slip along the thrust fault between 2 and 40 km depth. A tsunami in 1996, 200 km north of our site, was interpreted as being the result of an anomalously shallow interplate earthquake[2]. Seismic coupling at shallow depths, such as we observe, may explain why co-seismic events in the Peruvian subduction zone create large tsunamis.

In 2001, two precision transponder arrays were placed on the submarine portion of the South America plate, 20 and 50 km inland from the Peru–Chile trench axis. The objective was to precisely locate seafloor reference points over a two-year period, to calculate absolute horizontal deformation and model the updip limit of the seismogenic zone.

Andean subduction alternates between flat and steep slab subduction, based on the buoyancy of the oceanic crust as a result of age and thickness[3,4]. At 12° S, flat slab subduction causes the cold oceanic plate to extend hundreds of kilometres inland at about 100 km depth before descending. Earthquakes are created within the limits of the seismogenic zone, where converging plates are seismically coupled along the thrust. Tichelaar and Ruff[1] seismically located the downdip limit between 48 and 53 km in the flat slab region of Chile. The downdip limit is controlled by the 350 and 450 °C isotherms, in which crustal rocks begin stable sliding and reach the brittle–ductile transition[1,5,6]. Thermal models at various latitudes of the Chilean subduction zone show the 350 °C isotherm at a depth greater than 100 km as a result of flat subduction[1,4]. Oleskevich showed that for colder subducting plates, 40 km was still the downdip limit because of the intersection of the thrust fault and the continental forearc Moho. Hydrous minerals in the mantle wedge, such as serpentinite and talc, change the frictional properties and enable stable sliding. The Moho intersection occurs between 40 and 45 km depth or 200 km distance from the trench at 12° S. Land GPS measurements of surface deformation have been modelled to show a downdip limit of about 50 km (refs 7, 8).

The updip limit is controlled by the thickness of sediment going into the trench and the heat flow from the oceanic lithosphere. In the upper plate, unconsolidated sediments in the accretionary prism lack the strength to support a stress until sufficient cementation and consolidation has occurred. The stable to unstable sliding transition is thermally controlled and can be caused by dewatering of smectite to illite between 100 and 150 °C, opal alteration to quartz at 100 °C, low-grade metamorphic zeolite and calcite replacement of clay between 75 and 175 °C, pressure solution and quartz cementation above 150 °C and hydrocarbon migration in accretionary prisms between 100 and 150 °C (ref. 5). Thermal models of the flat subduction portion of the Chilean trench show a 100 °C isotherm at 7–12 km depth and 50 km from the trench. Seismology has been used to locate the updip limit in Costa Rica between 8 and 20 km depth, depending on heat flow and hydrothermal circulation[9].

A combination of GPS and acoustic travel times allow centimetre-level positioning of seafloor precision transponder arrays, a method shown in Fig. 1 (refs 10, 11). We collected 120 h of continuous 1-Hz GPS and acoustic data at the acoustic centre of two precision transponder arrays in 2001 and 2003. The amount of time required on site to obtain a repeatable solution is specific to the sea state, water properties, water depth and type of transponder used for this study. The resolution in the final position for the two arrays, for the two years, changes by less than ±10 mm after 80 h of data collection. We also collected conductivity–temperature–depth casts to calculate the ocean sound speed profile, and tide-gauge and

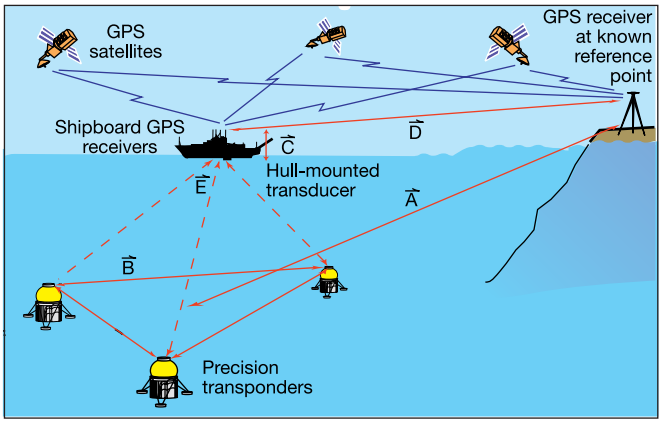

Figure 1 The GPS–acoustic approach to measure seafloor motion. Three precision transponders form an array with circle radius equal to the water depth. Relative transponder positions (**B**) are measured by acoustic ranges to a towed transducer (not shown). Dual-frequency 1-Hz GPS carrier phase data are collected at the ship and onshore (**D**). An optical survey connects phase centres from shipboard GPS antennas to the hull-mounted hydrophone (**C**). Two-way acoustic travel times are collected between the ship and transponder array (**E**). These vector components determine the horizontal components of **A**. Acoustic velocity variations do not bias the horizontal component of **A**.

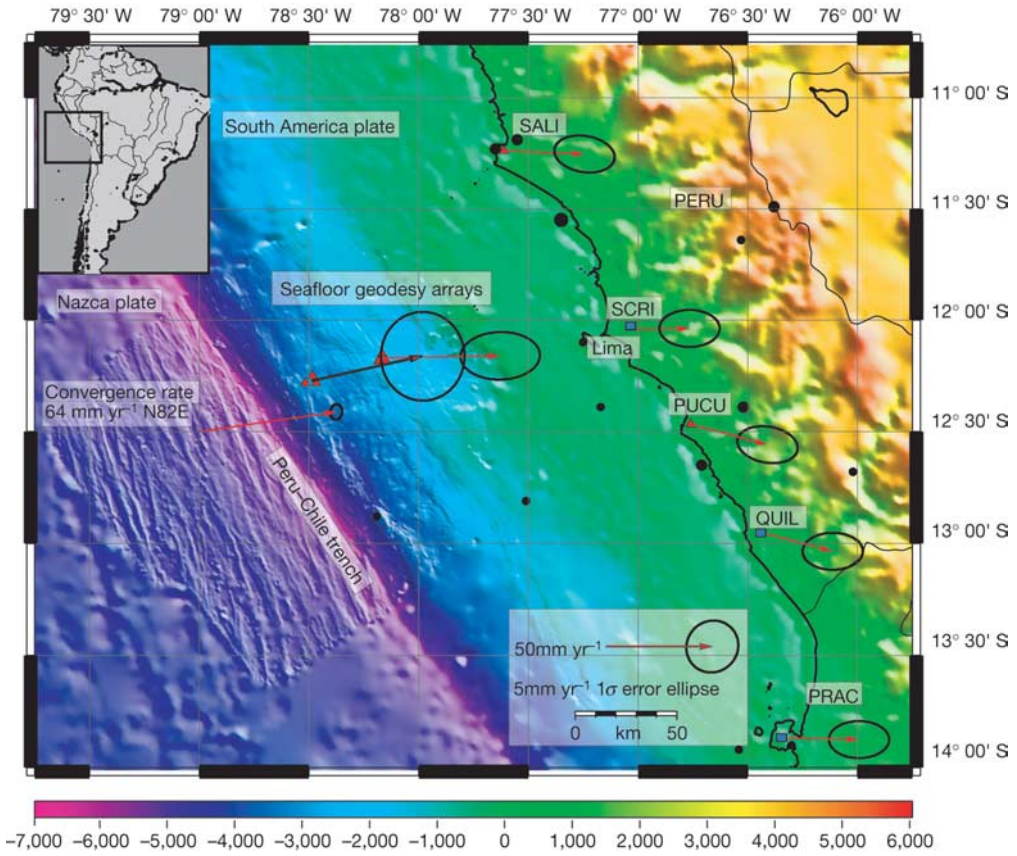

Figure 2 Bathymetric map of seafloor geodesy sites off the coast of Peru. Bathymetric data were collected in 2001 and 2003 from R/V *Roger Revelle* with SIMRAD EM 120. Circles represent earthquakes from the US Geological Survey/National Earthquake Information Center Preliminary Determinations of Epicenters solutions between data collection periods. The REVEL plate convergence vector (64 mm yr^{-1} at N 82° E) is shown relative to stable South America[17]. Vector solutions for Nazca convergence, temporary land stations and transponder arrays are shown relative to stable South America through the use of ITRF00 (ref. 25).

pressure-sensor data to calculate the depth of each transponder below sea level. Distant land GPS stations AREQ, BOGT, GALA, SANT, KOUR and FORT defined the ITRF 2000 reference frame for South America and were used to pinpoint the positions of three temporary 1-Hz GPS stations around Lima. These, in turn, were used to define the positions of three 1-Hz shipboard GPS antennas mounted on 12-m towers. GPS data were processed with the NASA Jet Propulsion Laboratories GIPSY OASIS II software[12]. Surveying techniques were employed on the ship to transfer the position of the hull-mounted transducer to the GPS antennas. The tower design and repetition of optical surveys ensure uncertainties of the order of millimetres[13]. After 100–120 h of data collection at each site in 2001 and 2003, the acoustically positioned seafloor transponders could be referenced to the motion of the stable craton.

The resulting trench perpendicular and parallel velocities of the high-rate land stations, land stations from ref. 8 and seafloor transponder arrays are shown in Fig. 2 and Table 1 (see also Supplementary Information).

An elastic dislocation model was created by using the program 3D-def from the University of Memphis, shown in Fig. 3a (ref. 14). The geometry of the thrust fault was based on refraction seismic profiles at 12° S from GEOPECO expeditions and referenced to seismic observations, Fig. 3b (refs 15, 16). The trench axis was chosen as the surface of the elastic halfspace, or 6 km below the sea surface. This will preserve the geometric and material properties of the two plates near the trench axis, the area of concern in this study. Two planes account for varying dip of the fault plane: 6° from 0–3 km and 10.5° to 60 km depth below the sea floor, or the bottom of the model profile. The displacement of elements along the fault was determined by using the components of the convergence vector perpendicular and parallel to the trench and in the downdip direction, 59 mm yr^{-1} downdip and 24 mm yr^{-1} along strike. The Sella calculation of the Nazca–South America Euler vector was used in this study for its comprehensive coverage. It was possible to compare each station velocity that defined the stable South American craton with those used in the Sella model. Euler predictions for Nazca–South America convergence range from 75 mm yr^{-1} at 81° (ref. 19), 68 mm yr^{-1} at 85° (ref. 20),

Table 1 **Velocities and 1σ errors of geodetic and transponder stations**

Station	Distance from trench axis (km)	Latitude	Longitude	Vector (mm yr^{-1})	Azimuth	Velocity (mm yr^{-1})	
						Trench perpendicular	Trench parallel
Convergence	–	11° 5.00′ S	79° 0.00′ W	64	N 82° E	60 ± 1	20 ± 1
SALI	150	11° 14.28′ S	77° 36.72′ W	37	N 92° E	31 ± 6	19 ± 4
SCRI	160	12° 2.40′ S	77° 1.80′ W	26	N 89° E	22 ± 5	13 ± 4
PUCU	170	12° 27.96′ S	76° 45.54′ W	37	N 105° E	26 ± 6	26 ± 4
QUIL	170	12° 57.00′ S	76° 26.40′ W	34	N 105° E	24 ± 5	24 ± 4
PRAC	130	13° 52.20′ S	76° 21.60′ W	37	N 91° E	32 ± 5	19 ± 4
Landward array	20	12° 10.09′ S	78° 9.92′ W	55	N 89° E	48 ± 7	26 ± 6
Seaward array	50	12° 16.36′ S	78° 29.18′ W	53	N 78° E	50 ± 7	15 ± 8

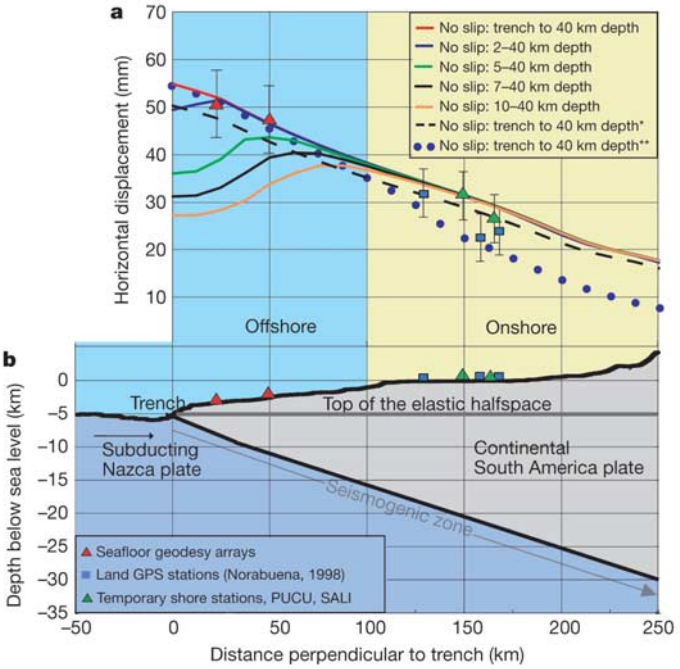

Figure 3 Models of surface deformation and plate organization. **a**, Modelling surface deformation: 3D-def model of the surface expression of a no-slip condition between the Nazca and South America plates. The onset of the no-slip zone was successively lowered from the trench to 10 km depth. Asterisk, model uses the convergence vector from ref. 20. Double asterisk, model uses a steeper dip. **b**, Plate organization: trench perpendicular profile from the Nazca to the South America plate around 12° S. Topography combines multibeam sonar and satellite altimetry data[26]. Displacement (and 1σ errors) perpendicular to the trench relative to stable South America are shown as triangles for temporary land stations and transponder arrays, and squares for land stations from ref. 8.

58 mm yr^{-1} at 80° (ref. 18), 64 mm yr^{-1} at 80° (ref. 7), to that used here, 64 mm yr^{-1} at 82° (ref. 17). The updip limit of the locked zone was successively lowered on the fault with each model and compared with the observed trench perpendicular velocities. Two additional models differed by using the convergence rate predicted in ref. 20 (model denoted by the asterisk) and the other by using a steeper dip as has been predicted by seismological results (denoted by two asterisks).

The measured horizontal surface motion perpendicular to the trench is consistent with a model having no slip along the thrust fault between 2 and 40 km depth[21]. It is possible that the mechanics of the wedge allow the no-slip condition to extend from 2 km depth up to the trench axis, but the data are unable to resolve the fault behaviour seaward of the two arrays. The shallower geometry of the thrust fault has been well determined by recent GEOPECO seismic refraction and reflection studies. Changes to the modelled fault geometry downdip of those do not affect the interpretation of the seafloor data. In addition, varying the convergence rate does not change the interpretation of the seafloor data. The far-field vector calculation for PUCU, SALI and rover stations support previously determined downdip locking at 40 km depth[8,22,23].

Tsunamigenic hazards investigated in ref. 2 present the 1996 earthquake and resulting tsunami 200 km north of our site as the result of an anomalously shallow, interplate earthquake 10 km below the sea floor. Citing examples from Nicaragua, Japan, Alaska and Peru, those authors show that the largest tsunamis are initiated by earthquakes below unconsolidated accretionary prisms. Evidence for continuous or episodic shallow locking may help to explain the "shallow extension of the seismogenic zone" that was suggested to have caused the Peruvian tsunami. The absence of slip at 2 km depth could mean that co-seismic events in the Peruvian subduction zone are more likely to create large tsunamis than subduction zones with deeper updip limits.

The updip limit can be compared with thermal models of flat slab subduction in Chile. There the convergence rate was 84 mm yr^{-1} and the plate age 45 Myr, whereas at 12° S the convergence rate used was 20 mm yr^{-1} slower and the plate age 35 Myr. The locations also differ in the amount of sediment accretion. Bounded by the Atacama Desert and the Mendaña fracture zone to the north, the trench south of 11.5° S has much less sediment input. In southern Chile, the sediment is several hundred metres thick and fed from the south[24]. Increased sediment and pore water may help to explain deeper estimates for the coupled zone in the southern portions of the trench. At 12° S, the small amount of trench sediment might increase the friction and decrease the depth of the seismogenic zone.

The deformation pattern of the defining Andean type margin has previously been confined to land-based GPS. Because the Peru–Chile trench is 150 km offshore, land-based methods are not sensitive to the activity of the plates near the trench. Seafloor geodesy, combing GPS and acoustics, and new seismic profiles revealing the upper geometry of the thrust fault, allow a previously unseen look at the initiation of a no-slip condition off the coast of Peru. The GPS/acoustic technique provides a method of measuring the convergence rate and increase in strain between plates that interact under water, which includes most plate boundaries around the world. □

Received 17 August 2004; accepted 27 January 2005; doi:10.1038/nature03412.

1. Tichelaar, B. W. & Ruff, L. J. Depth of seismic coupling along subduction zones. *J. Geophys. Res.* **98,** 2017–2037 (1993).
2. Satake, K. & Tanioka, Y. Sources of tsunami and tsunamigenic earthquakes in subduction zones. *Pure Appl. Geophys.* **154,** 467–483 (1999).
3. Cahill, T. & Isacks, I. Seismicity and shape of the subducted Nazca Plate. *J. Geophys. Res.* **97,** 17503–17529 (1992).
4. Gutscher, M. Andean subduction styles and their effect on thermal structure and interplate coupling. *J. S. Am. Earth Sci.* **15,** 3–10 (2002).
5. Moore, J. C. & Saffer, D. Updip limit of the seismogenic zone beneath the accretionary prism of southwest Japan: An effect of diagenetic to low-grade metamorphic processes and increasing effective stress. *Geology* **29,** 183–186 (2001).
6. Oleskevich, D. A., Hyndman, R. D. & Wang, K. The updip and downdip limits to great subduction earthquakes: Thermal and structural models of Cascadia, South Alaska, SW Japan, and Chile. *J. Geophys. Res.* **104,** 14965–14991 (1999).
7. Norabuena, E., Dixon, T. H., Stein, S. & Harrison, C. G. A. Decelerating Nazca–South America and Nazca–Pacific Plate motions. *Geophys. Res. Lett.* **26,** 3405–3408 (1999).
8. Norabuena, E. *et al.* Space geodetic observations of Nazca–South America convergence across the central Andes. *Science* **279,** 358–362 (1998).

9. Newman, A. V. *et al.* Along-strike variability in the seismogenic zone below Nicoya Peninsula, Costa Rica. *Geophys. Res. Lett.* **29,** 38–41 (2002).
10. Chadwell, C. D. & Bock, Y. Direct estimation of absolute precipitable water in oceanic regions by GPS tracking of a coastal buoy. *Geophys. Res. Lett.* **28,** 3701–3704 (2001).
11. Spiess, F. N. *et al.* Precise GPS/acoustic positioning of seafloor reference points for tectonic studies. *Physics Earth Planet. Inter.* **108,** 101–112 (1998).
12. Webb, F. H. & Zumberge, J. F. *An introduction to GIPSY/OASIS-II* (JPL Publication D-11088, Jet Propulsion Lab., Pasadena, California, 1997).
13. Chadwell, C. D. Shipboard towers for Global Positioning System antennas. *Ocean Eng.* **30,** 1467–1487 (2003).
14. Gomberg, J. & Ellis, M. Topography and tectonics of the central New Madrid seismic zone: Results of numerical experiments using a three-dimensional boundary-element program. *J. Geophys. Res.* **99,** 20299–20310 (1994).
15. Krabbenhöft, A., Bialas, J., Kopp, H., Kukowski, N. & Hübscher, C. Crustal structure of the Peruvian continental margin from wide-angle seismic studies. *Geophys. J. Int.* **159,** 749–764 (2004).
16. Hampel, A., Kukowski, N., Bialas, J., Huebscher, C. & Heinbockel, R. Ridge subduction at an erosive margin: The collision of the Nazca Ridge in southern Peru. *J. Geophys. Res.* **109,** B02101, doi:10.1029/2003JB002593 (2004).
17. Sella, G., Dixon, T. & Mao, A. REVEL: A model for recent plate velocites from space geodesy. *J. Geophys. Res.* **107,** 2081, doi:10.1029/2000JB00033 (2002).
18. Angermann, D. & Klotz, J. R. Space geodetic estimation of the Nazca–South America Euler vector. *Earth Planet. Sci. Lett.* **171,** 329–334 (1999).
19. DeMets, C., Gordon, R., Argus, D. & Stein, S. Effect of recent revision to the geomagnetic reversal time scale on estimates of current plate motion. *Geophys. Res. Lett.* **21,** 2191–2194 (1994).
20. Larson, K. M., Freymueller, J. T. & Philipsen, S. Global plate velocities from the Global Positioning System. *J. Geophys. Res.* **102,** 9961–9981 (1997).
21. Wang, K. & Dixon, T. "Coupling" semantics and science in earthquake research. *Eos* **85,** 180 (2004).
22. Tichelaar, B. & Ruff, L. Seismic coupling along the Chilean subduction zone. *J. Geophys. Res.* **96,** 11997–12022 (1991).
23. Bevis, M., Smalley, R. Jr, Herring, T., Godoy, J. & Galban, F. Crustal motion north and south of the Arica Deflection: Comparing recent geodetic results from the Central Andes. *Geochem. Geophys. Geosyst.* **1,** 1999GC000011 (1999).
24. Schweller, W. J., Kulm, L. D. & Prince, R. A. in *Nazca Plate: Crustal Formation and Andean Convergence* (eds Kulm, L. D., Dymond, J., Dasch, E. J., Hussong, D. M. & Roderick, R.) 323–349 (Mem. Geol. Soc. Am. 154, Geological Society of America, Boulder, Colorado, 1981).
25. Altimini, A., Sillard, P. & Boucher, C. ITRF2000: A new release of the International Terrestrial Reference Frame for earth science applications. *J. Geophys. Res.* **107,** 2214, doi:10.1029.2001JB000561 (2002).
26. Smith, W. H. F. & Sandwell, D. T. Global seafloor topography from satellite altimetry and ship depth soundings. *Science* **277,** 1957–1962 (1997).

Supplementary Information accompanies the paper on **www.nature.com/nature**.

Acknowledgements We thank M. Bevis for comments and suggestions; R. Zimmerman, D. Rimington and D. Price for engineering support; and the Captain and crew of the R/V *Roger Revelle*. We thank the Instituto Geofisico Del Peru for operating the land GPS stations and the Instituto Del Mar Del Peru, Direccion de Higrografia y Navagacion, for support at sea. This work was supported by the Marine Geology and Geophysics Program of the US National Science Foundation.

Competing interests statement The authors declare that they have no competing financial interests.

Correspondence and requests for materials should be addressed to C.D.C. (cchadwell@ucsd.edu).

Cycles in fossil diversity

Robert A. Rohde & Richard A. Muller

Department of Physics and Lawrence Berkeley Laboratory, University of California, Berkeley, California 94720, USA

It is well known that the diversity of life appears to fluctuate during the course of the Phanerozoic, the eon during which hard shells and skeletons left abundant fossils (0–542 million years ago). Here we show, using Sepkoski's compendium[1] of the first and last stratigraphic appearances of 36,380 marine genera, a strong 62 ± 3-million-year cycle, which is particularly evident in the shorter-lived genera. The five great extinctions enumerated by Raup and Sepkoski[2] may be an aspect of this cycle. Because of the high statistical significance we also consider the contributions of environmental factors, and possible causes.

Sepkoski's posthumously published *Compendium of Fossil Marine Animal Genera*[1], and its earlier versions, has frequently been used in the study of biodiversity and extinction[3,4]. For our purposes, diversity is defined as the number of distinct genera alive at any given time; that is, those whose first occurrence predates and whose last occurrence postdates that time. Because Sepkoski references only 295 stratigraphic intervals, the International Commission on Stratigraphy's 2004 time scale[5] is used to translate the stratigraphic references into a record of diversity versus time; details are given in the Supplementary Information. Although Sepkoski's is the most extensive compilation available, it is known to be subject to certain systematic limitations due primarily to the varying availability and quality of geological sections[6,7]. The implications of this will be discussed where appropriate.

Figure 1a shows a plot of diversity against time for all 36,380 genera in Sepkoski's *Compendium*. In Fig. 1b we show the 17,797 genera that remain when we remove those with uncertain ages (given only at epoch or period level), and those with only a single occurrence. The smooth trend curve through the data is the third-order polynomial that minimizes the variance of the difference

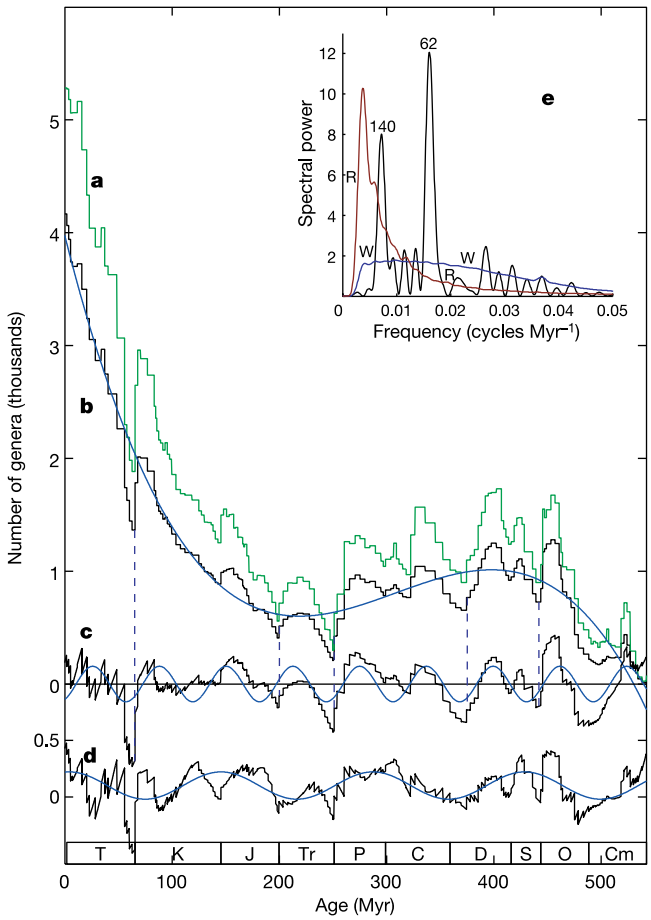

Figure 1 Genus diversity. **a**, The green plot shows the number of known marine animal genera versus time from Sepkoski's compendium[1], converted to the 2004 Geologic Time Scale[5]. **b**, The black plot shows the same data, with single occurrence and poorly dated genera removed. The trend line (blue) is a third-order polynomial fitted to the data. **c**, As **b**, with the trend subtracted and a 62-Myr sine wave superimposed. **d**, The detrended data after subtraction of the 62-Myr cycle and with a 140-Myr sine wave superimposed. Dashed vertical lines indicate the times of the five major extinctions[2]. **e**, Fourier spectrum of **c**. Curves W (in blue) and R (in red) are estimates of spectral background. Conventional symbols for major stratigraphic periods are shown at the bottom.